

# Delta-function-potential junctions with quasiparticles occupying tilted bands with quadratic-in-momentum dispersion

Ipsita Mandal\*

*Department of Physics, Shiv Nadar Institution of Eminence (SNIoE),  
Gautam Buddha Nagar, Uttar Pradesh 201314, India*

We continue our explorations of the transport characteristics in junction-configurations comprising semimetals with quadratic band-crossings, observed in the bandstructures of both two- and three-dimensional materials. Here, we consider short potential barriers/wells modelled by delta-function potentials. We also generalize our analysis by incorporating tilts in the dispersion. Due to the parabolic nature of the spectra, caused by quadratic-in-momentum dependence, there exist evanescent waves, which decay exponentially as we move away from the junction represented by the location of the delta-function potential. Investigating the possibility of the appearance of bound states, we find that their energies appear as pairs of  $\pm|E_b|$ , reflecting the presence of the imaginary-valued wavevectors at both positive and negative values of energies of the propagating quasiparticles.

## I. Introduction

Twofold- and multifold-degenerate points, caused by two or more bands crossing at specific points in the Brillouin zone (BZ), lead to the emergence of systems called nodal-point semimetals. Consequently, the density-of-states go exactly to zero right at the nodal points, and such a behaviour effectively falls in between that of metals (with bands overlapping in finite regions of the BZ) and insulators (with a finite gap between the bands everywhere). The nodal points, thus, represent Fermi points (rather than Fermi surfaces) when the chemical potential is adjusted to cut right at those points, and appear both in two-dimensional (2d) and three-dimensional (3d) materials. For example, graphene represents the 2d case when the honeycomb lattice is at half-filling, leading to 2d Dirac cones [1] in the BZ. Considering 3d, we are well-acquainted with the Dirac and Weyl semimetals [2]. While these well-known examples constitute the simplest cases of linear-in-momentum isotropic dispersion in the vicinity of the nodes, we are aware of bandstructures hosing anisotropic and/or nonlinear-in-momentum dispersion-directions. In particular, in this paper, we will focus on 2d and 3d semimetals hosting quadratic band-crossing points (QBCPs) [3–19], where a possible anisotropy appears in the parabolic-energy spectrum via tilting of the dispersion (with respect to a given momentum-axis). The 2d QBCPs are exemplified by bilayer graphene [20–22], and lattice structures of the checkerboard [3] (at half-filling), Kagome [3] (at one-third-filling), and Lieb [4] types. In 3d, materials like gapless semiconductors in the presence of a sufficiently strong spin-orbit coupling [23], gray tin ( $\alpha$ -Sn), mercury telluride (HgTe), and pyrochlore iridates (with the chemical formula  $A_2Ir_2O_7$ , where A stands for a lanthanide element [24, 25]) host parabolic spectra around nodal points. The 3d QBCPs have also been often dubbed as “Luttinger semimetals” in the literature, originating from the fact that their low-energy effective behaviour is captured by the so-called Luttinger Hamiltonian [6, 26–28].

In an earlier work [19], we have computed the transmission and reflection coefficients of the quasiparticles in the vicinity of 2d and 3d QBCPs, when moving across a rectangular potential barrier. Given the nonlinear-in momentum nature of the dispersion, there appear evanescent waves (see Refs. [29–32] for analogous situations in semimetals hosting hybrid dispersions depending on the momentum-axis considered). In this paper, we aim to chalk out analogous transport properties, but considering a delta-function-potential well/barrier. Additionally, we consider a tilt in the spectrum, which should exist in generic bandstructures. Plugging in the transmission amplitude ( $T$ ), the conductance ( $G$ ) is given by the Landauer formula of [33–35]

$$G = \frac{e^2}{2\pi\hbar} \sum_{\mathbf{n}} T_{\mathbf{n}}. \quad (1)$$

Here,  $e$  is the charge of one electron and  $\mathbf{n}$  labels the transverse momentum modes in the the strip of the material (in the experimental set-up). When an external potential difference  $\Phi$  is applied across a circuit, shot noise is the physical quantity which provides a measure of the fluctuations of the electric current-density away from its average value. At zero temperature, while the actual shot noise is defined by  $\mathcal{S} = \frac{e^3|\Phi|}{\pi\hbar} \sum_{\mathbf{n}} T_{\mathbf{n}}(1 - T_{\mathbf{n}})$ , the Poisson noise is given by the

---

\* ipsita.mandal@snu.edu.in

expression  $\mathcal{S}_P = \frac{e^3 |\Phi|}{\pi \hbar} \sum_{\mathbf{n}} T_{\mathbf{n}}$  [35]. The Poisson noise is the value of the noise that would be measured if the system produced noise due to quasiparticles carrying a single set of the relevant quantum numbers. A convenient measure of the sub-Poissonian shot noise is the Fano factor ( $F$ ), which is the ratio defined as [35]

$$F = \frac{\mathcal{S}}{\mathcal{S}_P} = \frac{\sum_{\mathbf{n}} T_{\mathbf{n}} (1 - T_{\mathbf{n}})}{\sum_{\tilde{\mathbf{n}}} T_{\tilde{\mathbf{n}}}}. \quad (2)$$

The paper is organized as follows. Secs. II and III deal with the 2d and 3d QBCPs, respectively. The representative characteristics of  $T$ ,  $G$ , and  $F$  are computed and compared with those of the free-electron gases. In Sec. IV, we venture into determining the energies of the bound states that may appear in our junction configurations. Finally, we conclude with a summary and outlook in Sec. V. In all our expressions, we resort to using the natural units, which indicates that the reduced Planck's constant ( $\hbar$ ), the speed of light ( $c$ ), and the magnitude of a single electronic charge ( $e$ ) are each set to unity.

## II. 2d QBCP

A QBCP in a 2d system harbours a twofold band-crossing, represented by the low-energy effective Hamiltonian [3],

$$\tilde{\mathcal{H}}_{2d}^{\text{kin}}(k_x, k_y) = \frac{1}{2m} [2 k_x k_y \sigma_x + (k_y^2 - k_x^2) \sigma_z] + \tilde{\eta} k_y \mathbb{I}_{2 \times 2}, \quad (3)$$

in the momentum space. Here, the second term represents a tilting of the dispersion with respect to the  $k_y$ -momentum direction. This Hamiltonian, with  $\tilde{\eta} = 0$ , also represents the chiral charge-carriers of bilayer-graphene [20–22].

For the sake of uncluttering of notations, we will divide all energies, momenta, and length-scales by the factors  $2m$ ,  $\sqrt{2m}$ , and  $1/\sqrt{2m}$ , respectively. Hence, we deal with the scaled Hamiltonian captured by

$$\mathcal{H}_{2d}^{\text{kin}}(k_x, k_y) = 2 k_x k_y \sigma_x + (k_y^2 - k_x^2) \sigma_z + \eta k_y \mathbb{I}_{2 \times 2}, \quad (4)$$

where the tilt parameter  $\eta = 2m \tilde{\eta}$ . The energy eigenvalues are captured by  $\eta k_y \pm \varepsilon_{2d}(k_x, k_y)$ , where

$$\varepsilon_{2d}(k_x, k_y) = k_x^2 + k_y^2, \quad (5)$$

where the “+” and “−” signs, in the usual conventions, refer to the positive-energy (or conduction) and negative-energy (or valence) bands, respectively. The corresponding orthonormal eigenvectors are given by

$$\Psi_+^T = \frac{1}{\sqrt{k_x^2 + k_y^2}} (k_y \quad k_x) \quad \text{and} \quad \Psi_-^T = \frac{1}{\sqrt{k_x^2 + k_y^2}} (-k_x \quad k_y), \quad (6)$$

respectively.

The 2d system is modulated by a delta-function-like electric potential barrier/well,

$$V(x) = V_0 \delta(x), \quad (7)$$

positioned at  $x = 0$ . Here,  $|V_0|$  reflects the strength of the potential barrier. Depending on whether  $V_0 > 0$  or  $V_0 < 0$ , we have either a barrier or a well. The total Hamiltonian for the entire configuration is captured by

$$\mathcal{H}_{2d}^{\text{tot}} = \mathcal{H}_{2d}^{\text{kin}}(-i \partial_x, -i \partial_y) + V(x), \quad (8)$$

when expressed in the position space. Here, we will consider the transport of quasiparticles along the  $x$ -axis, across the delta-function potential. We fix the Fermi-energy level at a value of  $E > 0$  in the region outside the potential barrier, which can be adjusted in an experimental set-up by either chemical doping or an external gate-voltage.

### A. Boundary conditions

For a material of a sufficiently large transverse dimension  $W$ , the boundary conditions are irrelevant for the bulk response. We use this freedom to impose periodic boundary conditions along the  $y$ -direction. Here, on a physical wavefunction  $\Psi^{\text{tot}}$  we impose periodic boundary conditions of  $\Psi^{\text{tot}}(x, W) = \Psi^{\text{tot}}(x, 0)$ . The transverse momentum  $k_y$  appears in the form of plane-wave solutions, leading to the ansatz for the  $k_y$ -dependent modes to behave as  $\sim e^{i k_y y}$ . Therefore, for a mode with

the transverse (to the propagation direction) momentum-component  $k_y$ , we must have  $|k_y| \leq \sqrt{E + \eta^2/4} - \eta/4$ . The  $k_x$ -components of the wavevectors of the incoming, reflected, and transmitted waves by solving  $E^2 = [k_x^2 + k_y(k_y + \eta)]^2 \Rightarrow k_x^2 = \pm E - k_y(k_y + \eta)$ . Consequently, in the regions  $x < 0$  and  $x > 0$ , this relation leads to the following four solutions:

$$k_x = \pm \sqrt{E - k_y(k_y + \eta)} \text{ and } k_x = \pm i \sqrt{E + k_y(k_y + \eta)}. \quad (9)$$

Due to the imaginary solutions, in addition to the propagating plane-waves, there exist evanescent waves [29–32] characterizing exponentially decaying amplitudes (as solutions with exponentially increasing amplitudes are physically inadmissible).

We follow usual procedure of matching the piecewise-continuous regions (see, e.g., Refs. [36, 37]) to compute the reflection and transport coefficients. Here, we consider the transport of positive energy states (i.e.,  $\Psi_+$ ) corresponding to electron-like particles. The transport of hole-like excitations (i.e.,  $\Psi_-$ ) will be similar. Hence, the Fermi level outside the potential barrier is adjusted to the value  $E$  (with  $E > 0$ ). A mode  $\sim \Psi_{k_y}(x) e^{i k_y y}$  is constructed in a piecewise fashion as

$$\Psi_{k_y}(x) = \begin{cases} \phi_L(x) & \text{for } x \leq 0 \\ \phi_R(x) & \text{for } x > 0 \end{cases}, \quad (10)$$

where

$$\begin{aligned} \phi_L(x) &= \frac{\Psi_+(k_{\text{in}}, k_y) e^{i k_{\text{in}} x} + r \Psi_+(-k_{\text{in}}, k_y) e^{-i k_{\text{in}} x}}{\sqrt{\mathcal{V}}} + \tilde{r} \Psi_-(-i \kappa, k_y) e^{-\kappa |x|}, \\ \phi_R(x) &= t \Psi_+(k_{\text{in}}, k_y) \frac{e^{i k_{\text{in}} x}}{\sqrt{\mathcal{V}}} + \tilde{t} \Psi_-(i \kappa, k_y) e^{-\kappa x}, \\ k_{\text{in}} &= \sqrt{E - k_y(k_y + \eta)}, \quad \mathcal{V} \equiv |\partial_{k_{\text{in}}} \varepsilon_{2d}(k_{\text{in}}, k_y)| = 2 k_{\text{in}}, \quad \kappa = \sqrt{E + k_y(k_y + \eta)}. \end{aligned} \quad (11)$$

Here, the magnitude of the group-velocity, captured by  $\mathcal{V}$ , is needed to define the scattering matrix comprising the transmission and reflection coefficients.

The boundary conditions can be obtained by integrating the equation  $\mathcal{H}_{2d}^{\text{tot}} \Psi^{\text{tot}} = E \Psi^{\text{tot}}$  over a small interval around  $x = 0$  in two consecutive steps. This amounts to imposing the continuity of the wavefunction and a constraint on its first-order derivatives (with respect to  $x$ ), as shown below:

$$\phi_L(0) = \phi_R(0) \text{ and } \partial_x \phi_R(x)|_{x=0} - \partial_x \phi_L(x)|_{x=0} = V_0 \phi_L(0). \quad (12)$$

These conditions are sufficient to guarantee the continuity of the flux of the probability-current density along the  $x$ -direction. From the matching of the wavefunction and its derivatives, we have two matrix-equations from the two boundary conditions. For 2d QPCBs, each of these matrix-equations can be separated into two components, since each wavevector has two components. Therefore, we have  $2 \times 2 = 4$  equations for the eight undetermined coefficients  $\{r, \tilde{r}, t, \tilde{t}\}$ .

## B. Transmission coefficients, conductance, and Fano factors

The explicit analytical expressions for  $t$  and  $r$  are shown below:

$$\begin{aligned} t &= 2 k_{\text{in}} \times \frac{\kappa^2 k_{\text{in}}^2 (2 \kappa + V_0) + 2 \kappa k_y^2 [\kappa (\kappa + V_0) - k_{\text{in}}^2] - [k_y^4 (2 \kappa + V_0)]}{[\kappa k_{\text{in}} (2 \kappa + V_0) - 2 k_{\text{in}} k_y^2 - i V_0 k_y^2] [k_y^2 (2 \kappa + V_0) + \kappa k_{\text{in}} (2 k_{\text{in}} + i V_0)]}, \\ r &= \frac{i V_0 (2 \kappa + V_0) (\kappa^2 k_{\text{in}}^2 + k_y^4)}{[\kappa k_{\text{in}} (2 \kappa + V_0) - 2 k_{\text{in}} k_y^2 - i V_0 k_y^2] [k_y^2 (2 \kappa + V_0) + \kappa k_{\text{in}} (2 k_{\text{in}} + i V_0)]}. \end{aligned} \quad (13)$$

For the untitled case (i.e.,  $\eta = 0$ ), we get

$$\begin{aligned} t &= \frac{4 E \cos \phi \sqrt{\sin^2 \phi + 1} - \sqrt{E} V_0 [\cos(3\phi) - 3 \cos \phi]}{\left[ V_0 \sin^2 \phi + \sqrt{\sin^2 \phi + 1} (2 \sqrt{E} + i V_0 \cos \phi) \right] \left[ \cos \phi (2 \sqrt{E} + V_0 \sqrt{\sin^2 \phi + 1}) - i V_0 \sin^2 \phi \right]}, \\ r &= \frac{i V_0 (2 \sqrt{E} \sqrt{\sin^2 \phi + 1} + V_0)}{\left[ V_0 \sin^2 \phi + \sqrt{\sin^2 \phi + 1} (2 \sqrt{E} + i V_0 \cos \phi) \right] \left[ \cos \phi (2 \sqrt{E} + V_0 \sqrt{\sin^2 \phi + 1}) - i V_0 \sin^2 \phi \right]}. \end{aligned} \quad (14)$$

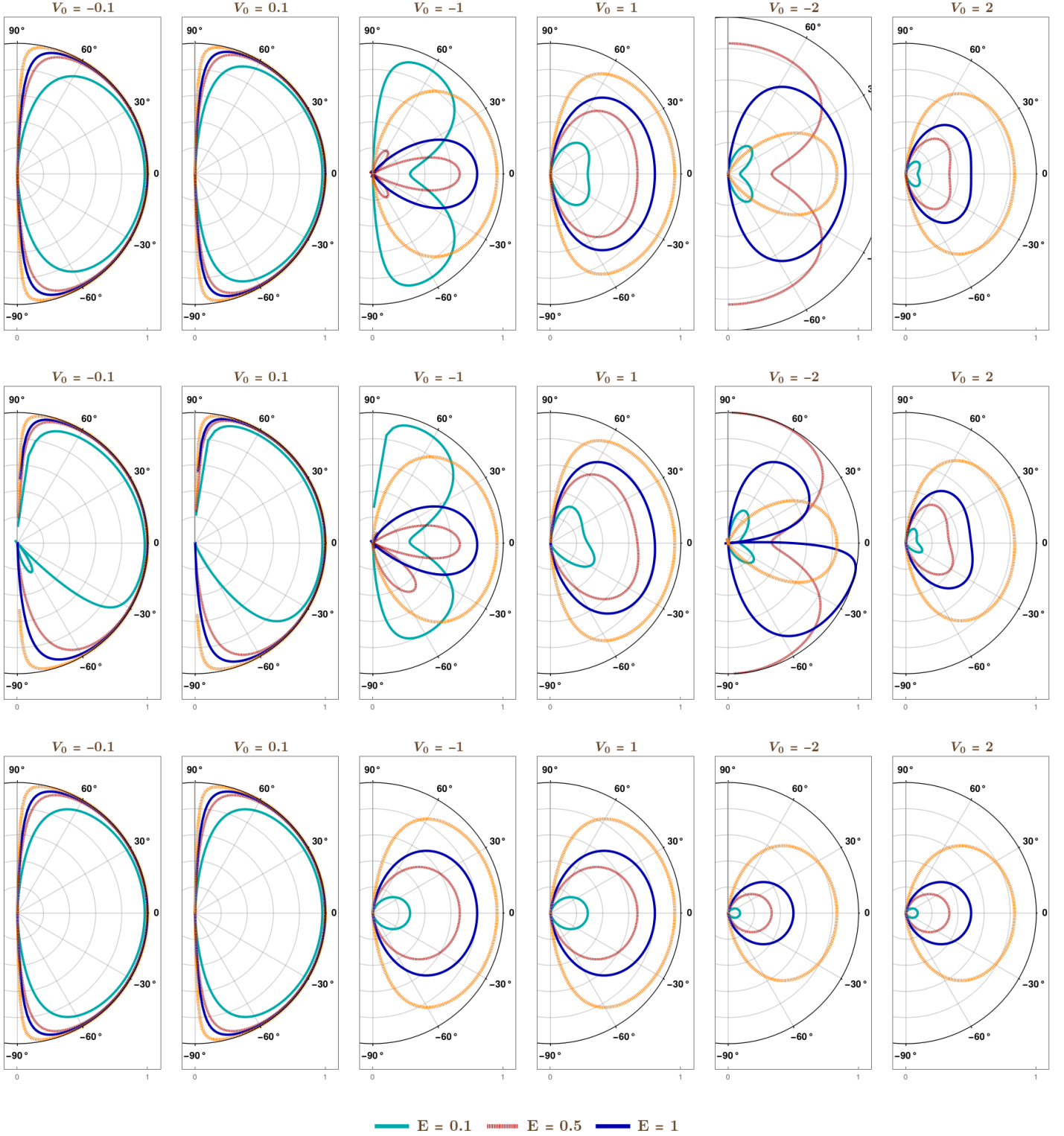


FIG. 1. Plots of the transmission coefficient ( $T$ ) as functions of the incident angle  $\phi$ , for various values of  $E$  and  $V_0$ . The subfigures in the uppermost, middle, and lowermost panels correspond to untitled 2d QBCP, tilted 2d QBCP with  $\eta = 0.25$ , and 2d electron-gas, respectively.

Because the evanescent-wave solutions decay off as we move away from the delta-function potential (at  $x = 0$ ), they do not contribute to the reflection and transmission coefficients. Hence, the transmission and reflection coefficients at an

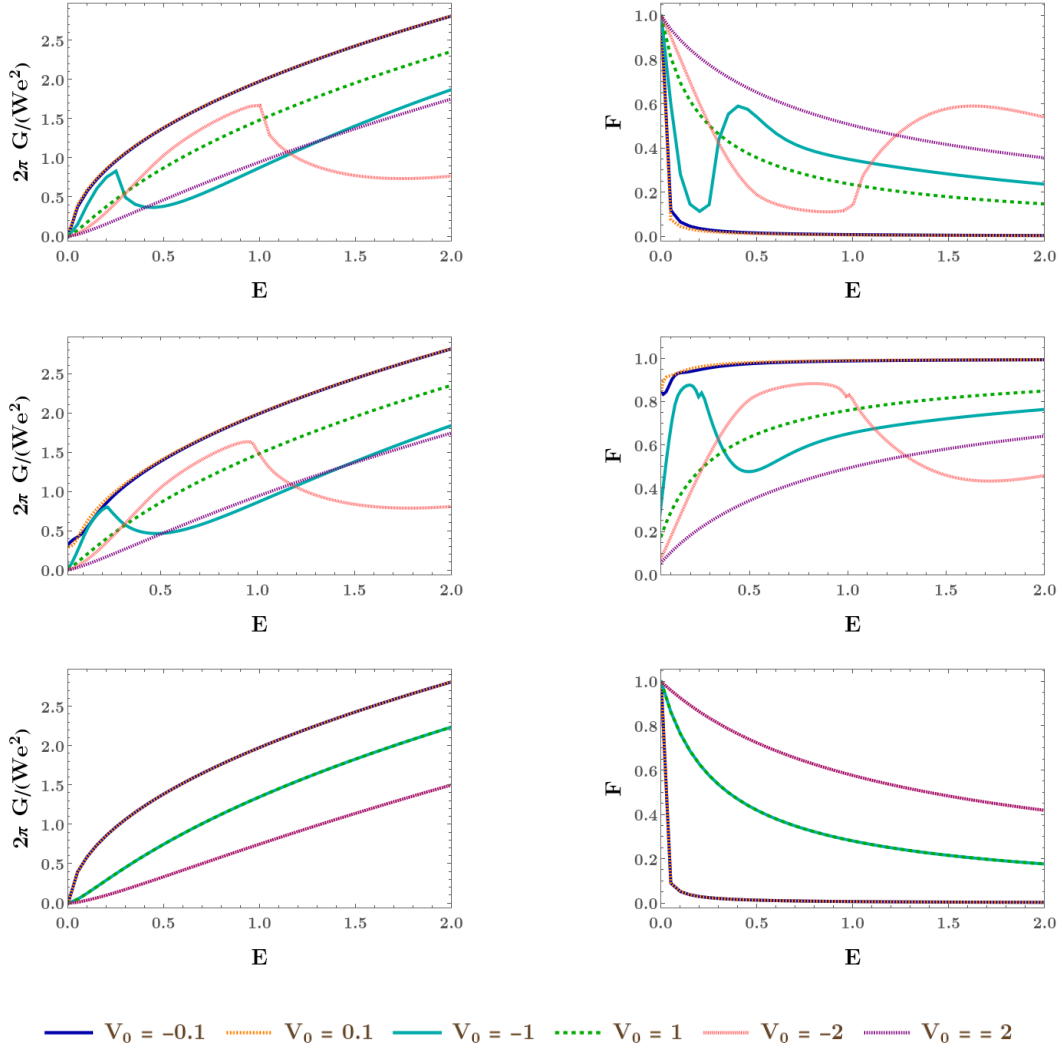


FIG. 2. Plots of the conductance ( $G$ ) and Fano factor ( $F$ ), as functions of  $E$ , for various values of  $V_0$ . The subfigures in the uppermost, middle, and lowest correspond to untitled 2d QBCP, tilted 2d QBCP with  $\eta = 0.25$ , and 2d electron-gas, respectively.

energy  $E$  are given by

$$T(E, V_0, \eta, \phi) = |t(E, V_0, \eta, \phi)|^2 \text{ and } R(E, V_0, \eta, \phi) = |r(E, V_0, \eta, \phi)|^2, \\ \text{with } \phi = \tan^{-1} \left( \frac{k_y}{\sqrt{E - k_y(k_y + \eta)}} \right). \quad (15)$$

Here,  $\phi$  denotes the incident angle of the incoming plane-wave. We represent the transmission-characteristics in the uppermost and middle panels of Fig. 1, with the help of polar plots. While the top panel captures the untitled case (i.e., with  $\eta = 0$ ), the middle panel corresponds to  $\eta = 0.25$ .

It is worthwhile to compare the results obtained above with those for a 2d electron-gas (since free electrons do have a quadratic-in momentum dispersion). For a delta-function barrier, it is well-known that the transmission amplitude and the transmission coefficient are given by

$$t(E, V_0, \phi) = \frac{2i\sqrt{E}\cos\phi}{V_0 + 2i\sqrt{E}\cos\phi} \Rightarrow T(E, V_0, \phi) = \frac{4E}{4E + V_0^2 \sec^2\phi}. \quad (16)$$

Fig. 1(b) illustrates the polar plots of the transmission coefficient. Comparing with Eqs. (13), we find that while the 2d transmission coefficient is insensitive to the sign of  $V_0$ , the behaviour for 2d QBCP changes as we switch the sign of  $V_0$  [cf. Fig. 1]

Let us assume  $W$  to be very large such that  $k_y$  can effectively be treated as a continuous variable. Taking the continuum limit corresponding to  $W \gg L$ , we consider the zero-temperature limit. Remembering that  $\hbar = 1$  in the natural units, the

conductance is given by [cf. Eq. (1)]

$$G(E, V_0) = \frac{e^2 W}{2\pi^2} \int_{-\sqrt{E+\frac{\eta^2}{4}-\frac{\eta}{2}}}^{\sqrt{E+\frac{\eta^2}{4}-\frac{\eta}{2}}} dk_y T(E, V_0, \eta, k_y). \quad (17)$$

In Fig. 2(a), we illustrate the conductance and the Fano factor [cf. Eq. (2)], as functions of  $E$ , for six different values of  $V_0$ . Side by side, the corresponding curves [generated using Eq. (16)] corresponding for a 2d electron-gas are provided in Fig. 2(b) for the sake of comparison.

### III. 3d QBCP

A QBCP in a 3d system harbours a fourfold band-crossing, where the four bands form a four-dimensional representation of the underlying lattice-symmetry group [8]. The effective continuum Hamiltonian, derived using the  $(\mathbf{k} \cdot \mathbf{p})$  method, is written down using a convenient representation of the five  $4 \times 4$  Euclidean Dirac matrices  $\Gamma_a$ , which is represented as [27, 28]

$$\tilde{\mathcal{H}}_{3d}^{\text{kin}}(k_x, k_y, k_z) = \frac{1}{2m} \sum_{a=1}^5 d_a(\mathbf{k}) \Gamma_a + \tilde{\eta} k_y \mathbb{I}_{4 \times 4}. \quad (18)$$

The  $\Gamma_a$ -matrices form one of the (two possible) irreducible four-dimensional Hermitian representations of the five-component Clifford algebra, defined by the anticommutator  $\{\Gamma_a, \Gamma_b\} = 2\delta_{ab}$ . The five anticommuting gamma-matrices can always be chosen such that three are real and two are imaginary [27, 38]. In the representation used here,  $(\Gamma_1, \Gamma_3, \Gamma_5)$  are real and  $(\Gamma_2, \Gamma_4)$  are imaginary:

$$\Gamma_1 = \sigma_1 \otimes \sigma_0, \quad \Gamma_2 = \sigma_2 \otimes \sigma_0, \quad \Gamma_3 = \sigma_3 \otimes \sigma_1, \quad \Gamma_4 = \sigma_3 \otimes \sigma_2, \quad \Gamma_5 = \sigma_3 \otimes \sigma_3. \quad (19)$$

The five functions  $d_a(\mathbf{k})$  are the real  $\ell = 2$  spherical harmonics (where  $\ell$  represents the angular-momentum channel), with the following structure:

$$d_1(\mathbf{k}) = \sqrt{3} k_y k_z, \quad d_2(\mathbf{k}) = \sqrt{3} k_x k_z, \quad d_3(\mathbf{k}) = \sqrt{3} k_x k_y, \quad d_4(\mathbf{k}) = \frac{\sqrt{3}}{2} (k_x^2 - k_y^2), \quad d_5(\mathbf{k}) = \frac{1}{2} (2k_z^2 - k_x^2 - k_y^2). \quad (20)$$

The second term in Eq. (18) represents a tilting of the dispersion with respect to the  $k_y$ -momentum direction.

Analogous to the 2d case, we will divide all energies, momenta, and length-scales by the factors  $2m$ ,  $\sqrt{2m}$ , and  $1/\sqrt{2m}$ , respectively. Hence, we deal with the scaled Hamiltonian captured by

$$\mathcal{H}_{3d}^{\text{kin}}(k_x, k_y, k_z) = \sum_{a=1}^5 d_a(\mathbf{k}) \Gamma_a + \eta k_y \mathbb{I}_{4 \times 4}, \quad (21)$$

whose energy eigenvalues are doubly-degenerate with the values  $\eta k_y \pm \varepsilon_{3d}(k_x, k_y, k_z)$ , with

$$\varepsilon_{3d}(k_x, k_y, k_z) = k_x^2 + k_y^2 + k_z^2. \quad (22)$$

The “+” and “−” signs, as usual, refer to the conduction and valence bands.

A set of orthonormal eigenvectors is given by the following:

$$\begin{aligned} \Psi_{+,1}^T &= \frac{1}{\mathcal{N}_{+,1}} \left( -\frac{(k_x + i k_y)(k + k_z)}{(k_x - i k_y)^2} \quad \frac{i(k + 3k_z)}{\sqrt{3}(k_x - i k_y)} \quad -\frac{i(-2k_z(k + k_z) + k_x^2 + k_y^2)}{\sqrt{3}(k_x - i k_y)^2} \quad 1 \right), \\ \Psi_{+,2}^T &= \frac{1}{\mathcal{N}_{+,2}} \left( \frac{(k_x + i k_y)(k - k_z)}{(k_x - i k_y)^2} \quad -\frac{i(k - 3k_z)}{\sqrt{3}(k_x - i k_y)} \quad -\frac{i(2k_z(k - k_z) + k_x^2 + k_y^2)}{\sqrt{3}(k_x - i k_y)^2} \quad 1 \right), \\ \Psi_{-,1}^T &= \frac{1}{\mathcal{N}_{-,1}} \left( -\frac{i(k + k_z)}{\sqrt{3}(k_x - i k_y)} \quad \frac{k - k_z}{k_x + i k_y} \quad 1 \quad -\frac{i(2k_z(k_z - k) + k_x^2 + k_y^2)}{\sqrt{3}(k_x + i k_y)^2} \right), \\ \Psi_{-,2}^T &= \frac{1}{\mathcal{N}_{-,2}} \left( \frac{i(k - k_z)}{\sqrt{3}(k_x - i k_y)} \quad -\frac{k + k_z}{k_x + i k_y} \quad 1 \quad -\frac{i(2k_z(k + k_z) + k_x^2 + k_y^2)}{\sqrt{3}(k_x + i k_y)^2} \right), \end{aligned} \quad (23)$$

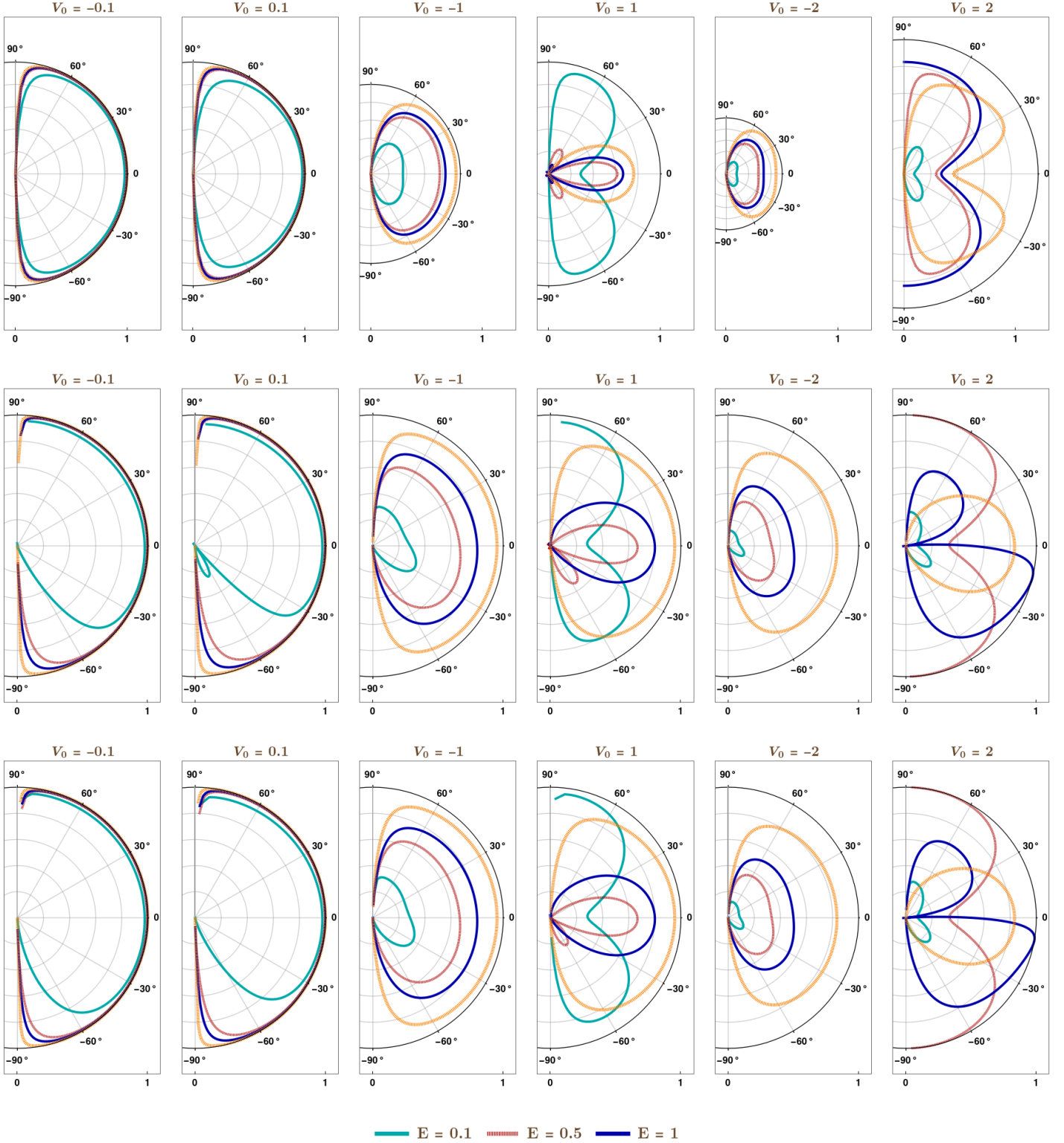


FIG. 3. Plots of the transmission coefficient ( $T$ ) as functions of the incident angle  $\theta$ , for various values of  $E$  and  $V_0$ . The subfigures in the uppermost, middle, and lowermost panels correspond to untitled 3d QBCP, tilted 3d QBCP with  $\{\eta, \phi\} = \{0.25, \pi/2\}$ , and tilted 3d QBCP with  $\{\eta, \phi\} = \{0.25, \pi/4\}$ , respectively.

where  $k = \sqrt{k_x^2 + k_y^2 + k_z^2}$ . The “+” (“-”) subscript indicates an eigenvector corresponding to the positive (negative) eigenvalue. The symbols  $\frac{1}{\mathcal{N}_{\pm,1}}$  and  $\frac{1}{\mathcal{N}_{\pm,2}}$  denote the corresponding normalization factors.

The 3d system is modulated by a delta-function-like electric potential barrier/well,

$$V(z) = V_0 \delta(z), \quad (24)$$

positioned at  $z = 0$ . Here, we choose the  $z$ -axis as the transport direction, and place the chemical potential at an energy  $E > 0$  in the regions outside the potential barrier. Since the tilt-axis is  $k_y$ , it does not matter whether we choose the propagation with respect to the  $k_x$ - or  $k_z$ -momentum — our choice here is merely a matter of convenience. As before, we need to consider the total Hamiltonian in the position space as

$$\mathcal{H}_{3d}^{\text{tot}} = \mathcal{H}_{3d}^{\text{kin}}(-i \partial_x, -i \partial_y, -i \partial_z) + V(z). \quad (25)$$

### A. Boundary conditions

We consider the tunneling in a slab of height and width  $W$ . Again, we assume that the material has a sufficiently large width  $W$  along each of the two transverse directions, such that the boundary conditions are irrelevant for the bulk response, thus allowing us to impose the following periodic boundary conditions:  $\tilde{\Psi}^{\text{tot}}(x, 0, z) = \tilde{\Psi}^{\text{tot}}(x, W, z)$  and  $\tilde{\Psi}^{\text{tot}}(0, y, z) = \tilde{\Psi}^{\text{tot}}(W, y, z)$ . The transverse momentum-components,  $k_x$  and  $k_y$ , are conserved, leading to modes with the dependence  $\sim e^{i k_x x} e^{i k_y y}$ . For any mode of a given value of the transverse-momentum components, we can determine the  $z$ -component of the wavevectors of the incoming, reflected, and transmitted waves (denoted by  $k_{\text{in}}$ ), by solving  $E^2 = [k_z^2 + k_x^2 + k_y^2 + \eta^2]^2 \Rightarrow k_z^2 = \pm E - k_{\perp} (k_{\perp} + \eta \sin \phi)$ , where  $k_x = k_{\perp} \cos \phi$  and  $k_y = k_{\perp} \sin \phi$ . Hence, we obtain the following four solutions:

$$k_z = \pm \sqrt{E - k_{\perp} (k_{\perp} + \eta \sin \phi)} \text{ and } k_z = \pm i \sqrt{E + k_{\perp} (k_{\perp} + \eta \sin \phi)}. \quad (26)$$

As we have understood by now from the 2d case, this implies the presence of the evanescent waves, corresponding to the imaginary solutions for  $k_z$ .

We will follow the same procedure as described for the 2d QBCP. Without any loss of generality, we consider the transport of one of the degenerate positive energy states,  $\Psi_{+,1}$ , corresponding to electron-like particles for one of the two degenerate conduction bands, with the Fermi level outside the potential barrier being adjusted to a value  $E = \varepsilon_{3d}(k_x, k_y, k_z)$ . In this case, a mode  $\sim \tilde{\Psi}_{k_x, k_y}(z) e^{i k_x x} e^{i k_y y}$  is constructed in a piecewise fashion as

$$\tilde{\Psi}_{k_x, k_y}(z) = \begin{cases} \tilde{\phi}_L(z) & \text{for } z \leq 0 \\ \tilde{\phi}_R(z) & \text{for } z > 0 \end{cases}, \quad (27)$$

where

$$\begin{aligned} \tilde{\phi}_L(z) &= \frac{\Psi_{+,1}(k_x, k_y, k_{\text{in}}) e^{i k_{\text{in}} z} + \sum_{s=1,2} r_s \Psi_{+,s}(k_x, k_y, -k_{\text{in}}) e^{-i k_{\text{in}} z}}{\sqrt{\tilde{\mathcal{V}}}} + \sum_{s=1,2} \tilde{r}_s \Psi_{-,s}(k_x, k_y, -i \kappa) e^{-\kappa |z|}, \\ \tilde{\phi}_R(z) &= \frac{\sum_{s=1,2} t_s \Psi_{+,s}(k_x, k_y, k_{\text{in}})}{\sqrt{\tilde{\mathcal{V}}}} e^{i k_{\text{in}} z} + \sum_{s=1,2} \tilde{t}_s \Psi_{-,s}(k_x, k_y, i \kappa) e^{\kappa z}, \\ k_{\text{in}} &= \sqrt{E - k_{\perp} (k_{\perp} + \eta \sin \phi)}, \quad \tilde{\mathcal{V}} \equiv |\partial_{k_{\text{in}}} \varepsilon_{3d}(k_x, k_y, k_{\text{in}})| = 2 k_{\text{in}}, \quad \kappa = \sqrt{E + k_{\perp} (k_{\perp} + \eta \sin \phi)}. \end{aligned} \quad (28)$$

Here, the magnitude of the group velocity, defined by  $\tilde{\mathcal{V}}$ , is needed to define the reflection and transmission coefficients appearing in the unitary scattering matrix.

The boundary conditions can be obtained by integrating the equation  $\mathcal{H}_{3d}^{\text{tot}} \tilde{\Psi}^{\text{tot}} = E \tilde{\Psi}^{\text{tot}}$  over a small interval around  $z = 0$  in two consecutive steps. This amounts to imposing the continuity of the wavefunction and a constraint on its first-order derivatives (with respect to  $z$ ), as shown below:

$$\tilde{\phi}_L(0) = \tilde{\phi}_R(0) \text{ and } \partial_z \tilde{\phi}_R(z)|_{z=0} - \partial_z \tilde{\phi}_L(z)|_{z=0} = V_0 \tilde{\phi}_L(0). \quad (29)$$

These conditions are sufficient to guarantee the continuity of the flux of the probability-current density along the  $z$ -direction. From the matching of the wavefunction and its derivatives, we have two matrix-equations from the two boundary conditions. For 3d QPCBs, each of these matrix-equations can be separated into four components, since each wavevector has four components. Therefore, we have  $2 \times 4 = 8$  equations for the eight undetermined coefficients  $\{r_1, r_2, \tilde{r}_1, \tilde{r}_2, t_1, t_2, \tilde{t}_1, \tilde{t}_2\}$ .

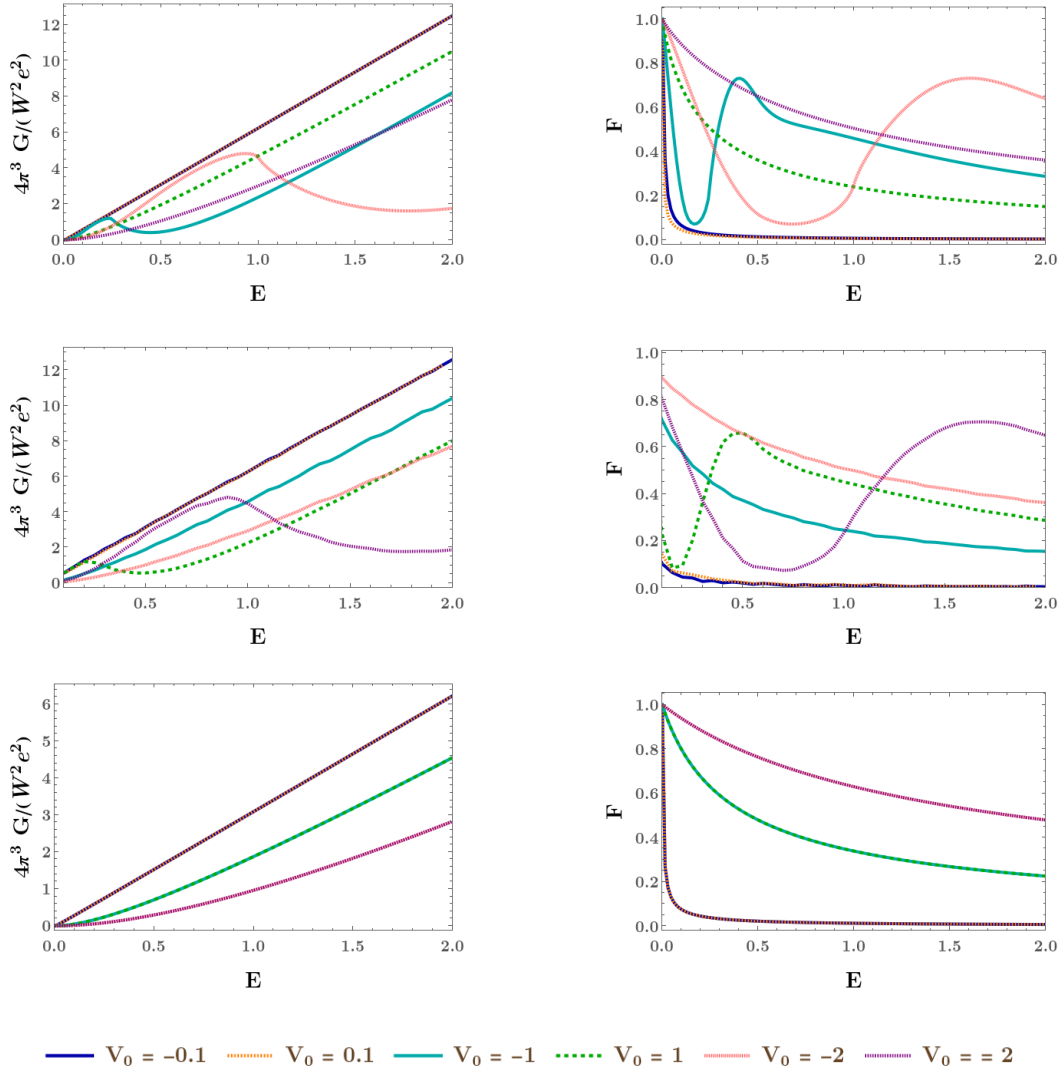


FIG. 4. Plots of the conductance ( $G$ ) and Fano factor ( $F$ ), as functions of  $E$ , for various values of  $V_0$ . The subfigures in the uppermost, middle, and lowest correspond to untitled 3d QBCP, tilted 3d QBCP with  $\eta = 0.25$ , and 3d electron-gas, respectively.

### B. Transmission coefficients, conductance, and Fano factors

The reflection and transmission coefficients at an energy  $E$  are given by

$$R(E, V_0, \eta, \theta, \phi) = |r_1(E, V_0, \eta, \theta, \phi)|^2 + |r_2(E, V_0, \eta, \theta, \phi)|^2 \text{ and } T(E, V_0, \eta, \theta, \phi) = |t_1(E, V_0, \eta, \theta, \phi)|^2 + |t_2(E, V_0, \eta, \theta, \phi)|^2, \quad (30)$$

with  $\theta = \tan^{-1} \left( k_{\perp} / \sqrt{E - k_{\perp}^2} (k_{\perp} + \eta \sin \phi) \right)$ .

Here,  $\theta$  defines the incident angle of the incoming wave. Although we have not provided the explicit expressions for  $t_1$  and  $t_2$ ,  $r_1$ , one can check that  $|t_2| = 0$  when the incident state is assumed to be  $\Psi_{+,1}$ .<sup>1</sup> Since the explicit analytical expressions for  $t_1$ ,  $t_2$ ,  $r_1$  and  $r_2$  are extremely long, we refrain from showing them here. Instead, we represent their characteristics via Fig. 3, with the help of polar plots representing  $T(E, V_0, \eta, \theta, \phi)$  as functions of  $\theta$ , picking some representative values of  $V_0$ ,  $E$ ,  $\eta$ , and  $\phi$ .

Again, we assume  $W$  to be very large such that  $k_x$  and  $k_y$  can effectively be treated as continuous variables. In the

<sup>1</sup> Similarly,  $|t_1| = 0$  when the incident state is assumed to be  $\Psi_{+,2}$ .

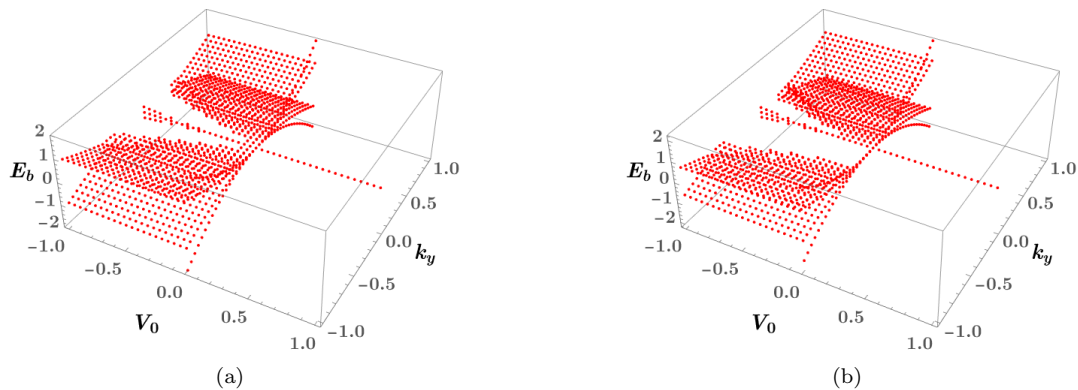


FIG. 5. Energies of the bound states ( $E_b$ ), as functions of  $V_0$  and  $k_y$ , for (a) an untilted 2d QBCP and (b) a tilted 2d QBCP with  $\eta = 0.25$ .

zero-temperature limit, the conductance is given by [cf. Eq. (1)]

$$G(E, V_0) = 2 \times \frac{e^2 W^2}{4 \pi^3} \int_0^{2\pi} d\phi \int_0^{\sqrt{E + \frac{\eta^2 \sin^2 \phi}{4} - \frac{\eta \sin \phi}{2}}} dk_{\perp} k_{\perp} T(E, V_0, \eta, k_{\perp}). \quad (31)$$

In order to account for the twofold degeneracy (since we have two independent conduction bands), we have included an extra factor of two. In Fig. 4, we illustrate the conductance and the Fano factor [using Eq. (2)], as functions of  $E$ , for six distinct values of  $V_0$ . The corresponding curves [generated using Eq. (16)] for a 3d electron-gas are also provided for the sake of comparison.

#### IV. Bound states

In this section, we focus on determining the nature of the bound states appearing in our junction set-ups for QBCPs. We denote their energy-values by  $E_b$ . We also discuss how the solutions differ from the solutions obtained for normal electron gases.

##### A. 2d QBCP

For the 2d case, we first define

$$\begin{aligned} \phi_L^b(x) &= r \Psi_{\zeta}(-k_{\text{in}}, k_y) e^{-i k_{\text{in}} x} + \tilde{r} \Psi_{-\zeta}(-i \kappa, k_y) e^{-\kappa |x|}, & \phi_R^b(x) &= t \Psi_{\zeta}(k_{\text{in}}, k_y) e^{i k_{\text{in}} x} + \tilde{t} \Psi_{-\zeta}(i \kappa, k_y) e^{-\kappa x}, \\ k_{\text{in}} &= \sqrt{|E| - k_y(k_y + \eta)}, & \kappa &= \sqrt{|E| + k_y(k_y + \eta)}, & \zeta &= \text{sgn}(E). \end{aligned} \quad (32)$$

Next, we need to impose the boundary conditions

$$\phi_L^b(0) = \phi_R^b(0) \text{ and } \partial_x \phi_R^b(x)|_{x=0} - \partial_x \phi_L^b(x)|_{x=0} = V_0 \phi_L^b(0), \quad (33)$$

leading to  $2 \times 2 = 4$  linear homogeneous equations for the four undetermined variables,  $\{r, \tilde{r}, t, \tilde{t}\}$ . Let  $\mathcal{M}_2$  denote the  $4 \times 4$  matrix constructed out of the four coefficients of these four variables. For the equations to be consistent, we need to impose the condition  $\det \mathcal{M}_2 = 0$ , whose solutions give us  $E = E_b$ . After some explicit calculations, we obtain

$$\det \mathcal{M}_2 = [k_y^2 (2 \kappa + V_0) - \kappa k_{\text{in}} (2 k_{\text{in}} + i V_0)] [V_0 k_y^2 - i k_{\text{in}} \{2 k_y^2 + \kappa (2 \kappa + V_0)\}]. \quad (34)$$

In comparison, the bound-state energies for a 2d electron gas is given by  $E_b = k_y^2 - V_0^2/4$ . From Eq. (34), we find that for  $k_y = 0$ , the bound states are given by  $E_b \in \{0, \pm V_0^2/4\}$ . Therefore, there are two points to observe for  $k_y = 0$ : (1) The bound states come with zero and positive values — in fact, the nonzero values come in pairs of  $\pm |E_b|$ . (2) There exists a bound state with  $E_b = 0$  irrespective of the value of  $V_0$ . The numerically-evaluated values of  $E_b$  are shown in Fig. 5, where the appearance of paired values in the form of  $\pm |E_b|$  is observed. This is no surprise because the existence of the evanescent waves reflect the existence of bound states with positive value as well. A point to note is that nonzero  $E_b$ -values exist only for  $V_0 < 0$ . For a nonzero  $\eta$ , an asymmetry with-respect-to the  $k_y$ -axis is observed, as expected from the tilting.

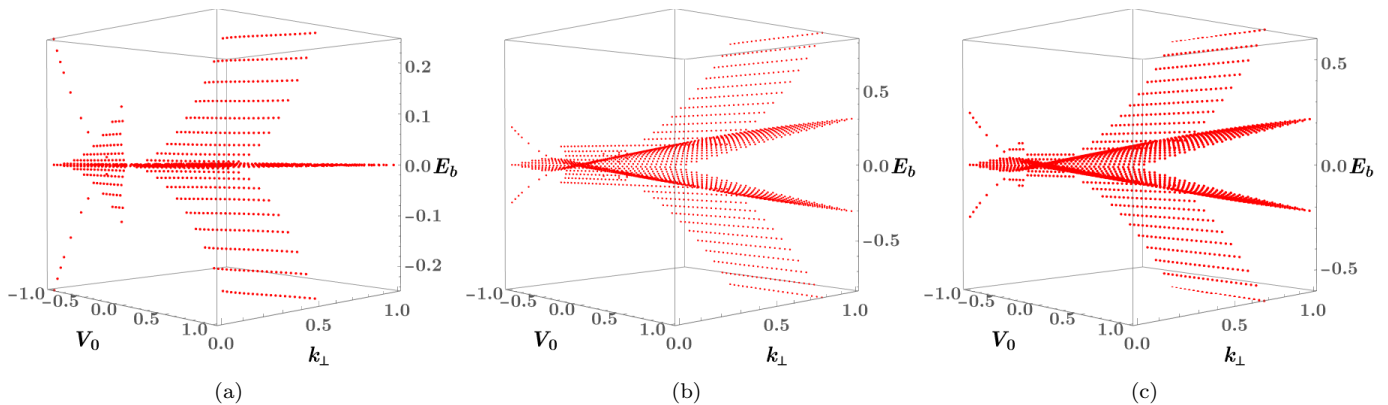


FIG. 6. Energies of the bound states ( $E_b$ ), as functions of  $V_0$  and  $k_\perp$ , for (a) an untilted 3d QBCP, (b) a tilted 3d QBCP with  $\{\eta, \phi\} = \{0.25, \pi/2\}$ , and (c) a tilted 3d QBCP with  $\{\eta, \phi\} = \{0.25, \pi/4\}$ .

### B. 3d QBCP

For the 3d case, we need to start with the definitions

$$\begin{aligned}\tilde{\phi}_L^b(z) &= \sum_{s=1,2} \left[ r_s \Psi_{\varsigma,s}(k_x, k_y, -k_{\text{in}}) e^{-i k_{\text{in}} z} + \tilde{r}_s \Psi_{-\varsigma,s}(k_x, k_y, -i \kappa) e^{-\kappa |z|} \right], \\ \tilde{\phi}_R^b(z) &= \sum_{s=1,2} \left[ t_s \Psi_{\varsigma,s}(k_x, k_y, k_{\text{in}}) e^{i k_{\text{in}} z} + \tilde{t}_s \Psi_{-\varsigma,s}(k_x, k_y, i \kappa) e^{\kappa z} \right], \\ k_{\text{in}} &= \sqrt{|E| - k_\perp (k_\perp + \eta \sin \phi)}, \quad \kappa = \sqrt{|E| + k_\perp (k_\perp + \eta)}, \quad \varsigma = \text{sgn}(E).\end{aligned}\quad (35)$$

Next, the boundary conditions of

$$\tilde{\phi}_L^b(0) = \tilde{\phi}_R^b(0) \text{ and } \partial_z \tilde{\phi}_R^b(z)|_{z=0} - \partial_z \tilde{\phi}_L^b(z)|_{z=0} = V_0 \tilde{\phi}_L^b(0), \quad (36)$$

provide us with  $2 \times 4 = 8$  equations for the eight undetermined variables,  $\{r_1, r_2, \tilde{r}_1, \tilde{r}_2, t_1, t_2, \tilde{t}_1, \tilde{t}_2\}$ . Let  $\mathcal{M}_3$  denote the  $8 \times 8$  matrix constructed out of the coefficients of these eight variables. For the equations to be consistent, we need to impose the condition  $\det \mathcal{M}_3 = 0$ , whose solutions give us  $E = E_b$ . After some explicit calculations, we arrive at

$$\begin{aligned}\det \mathcal{M}_3 &= \left[ -2 \kappa k_{\text{in}} k_\perp^2 (8 \kappa^2 + 7 \kappa V_0 + 3 V_0^2) + 2 k_{\text{in}}^3 \{k_\perp^2 (8 \kappa + V_0) - 4 \kappa^2 (2 \kappa + V_0)\} \right. \\ &\quad \left. + i V_0 k_{\text{in}}^2 \{k_\perp^2 (14 \kappa + V_0) - 4 \kappa^2 (2 \kappa + V_0)\} + 8 k_{\text{in}} k_\perp^4 (2 \kappa + V_0) + i V_0 k_\perp^2 (2 \kappa + V_0) (4 k_\perp^2 - \kappa^2) \right]^2.\end{aligned}\quad (37)$$

In comparison, the bound-state energies for a 3d electron gas is given by  $E_b = k_\perp^2 - V_0^2/4$ . Due to the overall square on the right-hand-side of Eq. (37), each  $E_b$  appears as a twofold-degenerate root, which results from the doubly-degenerate energy-bands of the parent Hamiltonian. In addition, we observe that for  $k_\perp = 0$ , the bound states are given by  $E_b \in \{0, \pm V_0^2/4\}$ , analogous to the 2d case. In general, the evanescent waves result in the solutions appearing as  $\pm E_b$  for generic values of  $V_0$ ,  $k_\perp$ , and  $\phi$ . This is reflected in Fig. 6, where the values of  $E_b$  are shown for some representative parameter-values. Contrasting with the 2d case, we find that nonzero values of  $E_b$  appear even for  $V_0 > 0$ .

### V. Summary and outlook

In this paper, we have elucidated the transmission characteristics of quasiparticles for generic tilted QBCPs, while travelling across a delta-function potential barrier/well. Compared to nodal-point semimetals harbouring linear-in-momentum band-crossings, the novelty of a parabolic spectrum is reflected by the necessity to include solutions comprising evanescent waves. The existence of these imaginary-wavevector solutions give rise to bound states appearing as pairs of  $\pm |E_b|$ . We would like to emphasize that such exponentially-decaying solutions do not appear for the case of linear-in-momentum dispersive spectra, for example, which appear in Dirac cones of graphene [22, 39], pseudospin-1 (or triple-point) semimetals [40–42], Rarita-Schwinger-Weyl semimetals [42], and Weyl semimetals [29, 30, 43, 44]. A nonzero tilt makes the situation

even richer, with the tilt-anisotropy being reflected in anisotropies in the transmission coefficients as well as the distribution of the bound states with respect to the values of the  $k_y$ -momentum. Twofold-degeneracy of the eigenvalues of the Hamiltonian in 3d QBCP result in the bound-state energies being doubly-degenerate as well. Analogous systems with nonlinear momentum dependence include semi-Dirac semimetals [31, 32] and multi-Weyl semimetals [29, 30, 44].

In the future, it will be worthwhile to investigate the nature of Andreev bound states and their contributed currents in Josephson junctions constructed out of the 2d and 3d QBCPs. This will be in the same spirit as has been for materials such as graphene, Weyl/multi-Weyl semimetals, semi-Dirac semimetals, pseudospin-1 semimetals, and Rarita-Schwinger-Weyl semimetals [32, 45–48]. However, the calculations will be significantly more challenging because of the proliferation of the number of undetermined coefficients, caused by the overarching presence of the evanescent waves.

### Data availability

Data sharing is not applicable to this article as no new data were created or analyzed in this study.

- 
- [1] A. H. Castro Neto, F. Guinea, N. M. R. Peres, K. S. Novoselov, and A. K. Geim, The electronic properties of graphene, *Rev. Mod. Phys.* **81**, 109 (2009).
  - [2] N. P. Armitage, E. J. Mele, and A. Vishwanath, Weyl and dirac semimetals in three-dimensional solids, *Rev. Mod. Phys.* **90**, 015001 (2018).
  - [3] K. Sun, H. Yao, E. Fradkin, and S. A. Kivelson, Topological insulators and nematic phases from spontaneous symmetry breaking in 2D Fermi systems with a quadratic band crossing, *Phys. Rev. Lett.* **103**, 046811 (2009).
  - [4] W.-F. Tsai, C. Fang, H. Yao, and J. Hu, Interaction-driven topological and nematic phases on the lieb lattice, *New Journal of Physics* **17**, 055016 (2015).
  - [5] I. Mandal and S. Gemsheim, Emergence of topological Mott insulators in proximity of quadratic band touching points, *Condensed Matter Physics* **22**, 13701 (2019).
  - [6] A. A. Abrikosov, Calculation of critical indices for zero-gap semiconductors, *JETP* **39**, 709 (1974).
  - [7] T. Kondo, M. Nakayama, R. Chen, J. J. Ishikawa, E. G. Moon, T. Yamamoto, Y. Ota, W. Malaeb, H. Kanai, Y. Nakashima, Y. Ishida, R. Yoshida, H. Yamamoto, M. Matsunami, S. Kimura, N. Inami, K. Ono, H. Kumigashira, S. Nakatsuji, L. Balents, and S. Shin, Quadratic fermi node in a 3d strongly correlated semimetal, *Nat. Commun.* **6** (2015).
  - [8] E.-G. Moon, C. Xu, Y. B. Kim, and L. Balents, Non-Fermi-liquid and topological states with strong spin-orbit coupling, *Phys. Rev. Lett.* **111**, 206401 (2013).
  - [9] R. M. Nandkishore and S. A. Parameswaran, Disorder-driven destruction of a non-Fermi liquid semimetal studied by renormalization group analysis, *Phys. Rev. B* **95**, 205106 (2017).
  - [10] I. Mandal and R. M. Nandkishore, Interplay of Coulomb interactions and disorder in three-dimensional quadratic band crossings without time-reversal symmetry and with unequal masses for conduction and valence bands, *Phys. Rev. B* **97**, 125121 (2018).
  - [11] I. Mandal, Tunneling in Fermi systems with quadratic band crossing points, *Annals of Physics* **419**, 168235 (2020).
  - [12] B. Cheng, T. Ohtsuki, D. Chaudhuri, S. Nakatsuji, M. Lippmaa, and N. Armitage, Dielectric anomalies and interactions in the three-dimensional quadratic band touching Luttinger semimetal  $\text{Pr}_2\text{Ir}_2\text{O}_7$ , *Nat. Commun.* **8**, 2097 (2017).
  - [13] I. Mandal and H. Freire, Transport in the non-Fermi liquid phase of isotropic Luttinger semimetals, *Phys. Rev. B* **103**, 195116 (2021).
  - [14] H. Freire and I. Mandal, Thermoelectric and thermal properties of the weakly disordered non-Fermi liquid phase of Luttinger semimetals, *Physics Letters A* **407**, 127470 (2021).
  - [15] I. Mandal and H. Freire, Raman response and shear viscosity in the non-Fermi liquid phase of Luttinger semimetals, *Journal of Physics: Condensed Matter* **34**, 275604 (2022).
  - [16] I. Mandal, Search for plasmons in isotropic Luttinger semimetals, *Annals of Physics* **406**, 173 (2019).
  - [17] J. Wang and I. Mandal, Anatomy of plasmons in generic Luttinger semimetals, *Eur. Phys. J. B* **96**, 132 (2023).
  - [18] S. Bera and I. Mandal, Floquet scattering of quadratic band-touching semimetals through a time-periodic potential well, *J. Phys. Condens. Matter* **33**, 295502 (2021).
  - [19] I. Mandal, Transmission through rectangular potentials in semimetals featuring quadratic dispersion, *arXiv e-prints* (2025), [arXiv:2502.06265 \[cond-mat.mes-hall\]](https://arxiv.org/abs/2502.06265).
  - [20] E. McCann and V. I. Fal'ko, Landau-level degeneracy and quantum Hall effect in a graphite bilayer, *Phys. Rev. Lett.* **96**, 086805 (2006).
  - [21] K. S. Novoselov, E. McCann, S. V. Morozov, V. I. Fal'ko, M. I. Katsnelson, U. Zeitler, D. Jiang, F. Schedin, and A. K. Geim, Unconventional quantum Hall effect and Berry's phase of  $2\pi$  in bilayer graphene, *Nature Physics* **2**, 177 (2006).
  - [22] M. I. Katsnelson, K. S. Novoselov, and A. K. Geim, Chiral tunnelling and the Klein paradox in graphene, *Nature Physics* **2**, 620 (2006).
  - [23] A. A. Abrikosov and S. D. Beneslavskii, Possible existence of substances intermediate between metals and dielectrics, *Soviet Journal of Experimental and Theoretical Physics* **32**, 699 (1971).
  - [24] D. Yanagishima and Y. Maeno, Metal-nonmetal changeover in pyrochlore iridates, *Journal of the Physical Society of Japan* **70**, 2880 (2001).

- [25] K. Matsuhira, M. Wakeshima, R. Nakanishi, T. Yamada, A. Nakamura, W. Kawano, S. Takagi, and Y. Hinatsu, Metal–insulator transition in pyrochlore iridates  $\text{Ln}_2\text{Ir}_2\text{O}_7$  ( $\text{Ln} = \text{Nd}, \text{Sm}, \text{and Eu}$ ), *Journal of the Physical Society of Japan* **76**, 043706 (2007).
- [26] J. M. Luttinger, Quantum theory of cyclotron resonance in semiconductors: General theory, *Phys. Rev.* **102**, 1030 (1956).
- [27] S. Murakami, N. Nagaosa, and S.-C. Zhang,  $\text{SU}(2)$  non-Abelian holonomy and dissipationless spin current in semiconductors, *Phys. Rev. B* **69**, 235206 (2004).
- [28] I. Boettcher and I. F. Herbut, Superconducting quantum criticality in three-dimensional Luttinger semimetals, *Phys. Rev. B* **93**, 205138 (2016).
- [29] Y.-H. Deng, H.-F. Lü, S.-S. Ke, Y. Guo, and H.-W. Zhang, Quantum tunneling through a rectangular barrier in multi-Weyl semimetals, *Phys. Rev. B* **101**, 085410 (2020).
- [30] I. Mandal and A. Sen, Tunneling of multi-Weyl semimetals through a potential barrier under the influence of magnetic fields, *Physics Letters A* **399**, 127293 (2021).
- [31] S. Banerjee, R. R. P. Singh, V. Pardo, and W. E. Pickett, Tight-binding modeling and low-energy behavior of the semi-Dirac point, *Phys. Rev. Lett.* **103**, 016402 (2009).
- [32] I. Mandal, Andreev bound states in Josephson junctions of semi-Dirac semimetals, *Physica B: Condensed Matter* **683**, 415918 (2024).
- [33] R. Landauer, Spatial variation of currents and fields due to localized scatterers in metallic conduction (and comment), *Journal of Mathematical Physics* **37**, 5259 (1996).
- [34] M. Büttiker, Quantized transmission of a saddle-point constriction, *Phys. Rev. B* **41**, 7906 (1990).
- [35] Y. Blanter and M. Büttiker, Shot noise in mesoscopic conductors, *Physics Reports* **336**, 1 (2000).
- [36] M. Salehi and S. Jafari, Quantum transport through 3D Dirac materials, *Annals of Physics* **359**, 64 (2015).
- [37] J. Tworzydło, B. Trauzettel, M. Titov, A. Rycerz, and C. W. J. Beenakker, Sub-Poissonian shot noise in graphene, *Phys. Rev. Lett.* **96**, 246802 (2006).
- [38] I. F. Herbut, Isospin of topological defects in Dirac systems, *Phys. Rev. B* **85**, 085304 (2012).
- [39] P. E. Allain and J. N. Fuchs, Klein tunneling in graphene: optics with massless electrons, *The European Physical Journal B* **83**, 301–317 (2011).
- [40] A. Fang, Z. Q. Zhang, S. G. Louie, and C. T. Chan, Klein tunneling and supercollimation of pseudospin-1 electromagnetic waves, *Phys. Rev. B* **93**, 035422 (2016).
- [41] R. Zhu and P. M. Hui, Shot noise and Fano factor in tunneling in three-band pseudospin-1 Dirac–Weyl systems, *Physics Letters A* **381**, 1971 (2017).
- [42] I. Mandal, Transmission in pseudospin-1 and pseudospin-3/2 semimetals with linear dispersion through scalar and vector potential barriers, *Physics Letters A* **384**, 126666 (2020).
- [43] C. Yesilyurt, S. G. Tan, G. Liang, and M. B. A. Jalil, Klein tunneling in Weyl semimetals under the influence of magnetic field, *Scientific Reports* **6**, 38862 (2016).
- [44] I. Mandal, Transmission and conductance across junctions of isotropic and anisotropic three-dimensional semimetals, *European Physical Journal Plus* **138**, 1039 (2023).
- [45] M. Maiti and K. Sengupta, Josephson effect in graphene superconductor/barrier/superconductor junctions: Oscillatory behavior of the Josephson current, *Phys. Rev. B* **76**, 054513 (2007).
- [46] K. Kulikov, D. Sinha, Y. M. Shukrinov, and K. Sengupta, Josephson junctions of Weyl and multi-Weyl semimetals, *Phys. Rev. B* **101**, 075110 (2020).
- [47] I. Mandal, Andreev bound states in superconductor-barrier-superconductor junctions of Rarita-Schwinger-Weyl semimetals, *Physics Letters A* **503**, 129410 (2024).
- [48] I. Mandal, Nature of Andreev bound states in Josephson junctions of triple-point semimetals, *arXiv e-prints* (2024), [arXiv:2406.15350](https://arxiv.org/abs/2406.15350) [cond-mat.supr-con].